Electronic Supplementary Material (ESI) for ChemComm.
This journal is © The Royal Society of Chemistry 2019

Electronic Supplementary Information

Small graphite nanoflakes as an advanced cathode material for aluminum ion batteries

Haoyu Hu, ‡[a] Tonghui Cai, ‡[b] Peng Bai,[a] Jing Xu,[a] Shihui Ge,[a] Han Hu,[b] Mingbo Wu,[b] Qingzhong Xue,[a,b] Zifeng Yan,[a] Xiuli Gao,*[b] Wei Xing *[a,b]

[a] State Key Laboratory of Heavy Oil Processing, School of Material Science and Engineering, China University of Petroleum, Qingdao 266580 (P. R. China) E-mail: xingwei@upc.edu.cn

[b] Institute of New Energy, China University of Petroleum, Qingdao 266580 (P. R. China) xlgao@upc.edu.cn

Experimental

Reagents and materials. The raw materials, natural flake graphite (≥99.9%,≥325 mesh), 1-methyl-2-pyrrolidinone (NMP, ≥ 99%), 1-ethyl-3-methylimidazolium chloride ([EMIm]Cl, 98%) and aluminum chloride ($AlCl_3$, 99%) were purchased from Aladdin Industrial Corporation (Shanghai, China). Polyvinylidene fluoride (PVDF), hexadecyl trimethyl ammonium bromide (CTAB,≥99.0%) and absolute ethanol (≥ 99.7%) were commercially available from Sinopharm Chemical Reagent Co., Ltd (Shanghai, China). All chemicals were used without further purification, and the water used in the experiment was deionized water.

The preparation of small graphite nanoflakes. Natural flake graphite and PVDF were ground in an agate mortar at a mass ratio of 9:1, and NMP was added to prepare a slurry. The slurry was then uniformly coated on a copper foil and dried at 60 °C for 8 h. The copper foil was then cut into discs that was assembled into a button cell using a lithium foil as the counter electrode. The button cell was then discharged to 0.005 V at a current density of 100 mA/g. Afterwards, the graphite-coated copper disc was taken out from the button cell and placed in a 17.8 mmol/L CTAB solution. After reacting violently with water, the solution was ultrasonicated for 1 h. Finally, the obtained suspension was vacuum-filtered, washed with ethanol several times, and dried at 60 °C overnight. The final product was designated as SGN.

Materials characterizations. The crystal structure of the samples were measured by powder X-ray diffraction (XRD, D8 Advance, Germany) using Cu Kα radiation (λ = 0.15418 nm) at 40 kV, 30 mA, with a scan step of 0.02° and a 2 theta angle ranging from 5 to 75°. The morphology of the sample was characterized by field emission scanning electron microscope (SEM, JSM-7900F, JEOL, Japan) with an energy dispersive X-ray spectrometry analyzer (EDS). The microstructure of the sample was further observed by transmission electron microscopy (TEM, FEI, Tecnai G2 20 S-TWIN). Raman spectroscope (DXR, Thermo Fisher Scientific) was used to characterize the structure of carbon skeleton for the samples. Thermogravimetric ananlysis (TGA) of the samples was conducted with air flow (cm^3/min) on a synchronous thermal analyzer (SDT650, NETZSCH, Germany).

Electrochemical measurements. The active material (SGN) and polyvinylidene fluoride binder (PVDF) were grinded in an agate mortar at a mass ratio of 9:1, and then uniformly mixed with NMP for 1 h under ultrasound to obtain a uniform slurry. An electrode was made by coating the slurry onto molybdenum foil and drying at 60 °C overnight. A custom Swagelok cell was then assembled by using the SGN electrode as positive electrode, Al foil as negative electrode, and $AlCl_3$/[EMIm]Cl as electrolyte. To clearly show that there is no side reaction caused by this custom Swagelok cell, we first evaluated the error that may be introduced by the Swagelok cell. Cyclic voltammetry (CV) and electrochemical impedance spectroscopy (EIS) were conducted on a CHI 660E electrochemical workstation. Galvanostatic charge-discharge (GCD) measurements and the galvanostatic intermittent titration technique (GITT) measurements were carried out on a LAND battery tester.

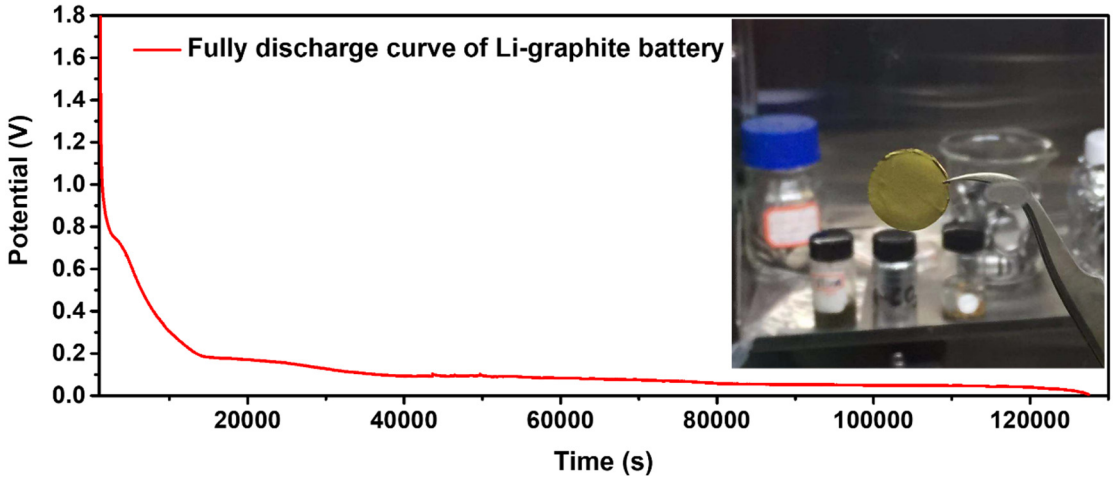

Fig. S1. The discharge curve of natural graphite in the Li-graphite battery and the color change of anode when discharged to 0.005 V (the inset).

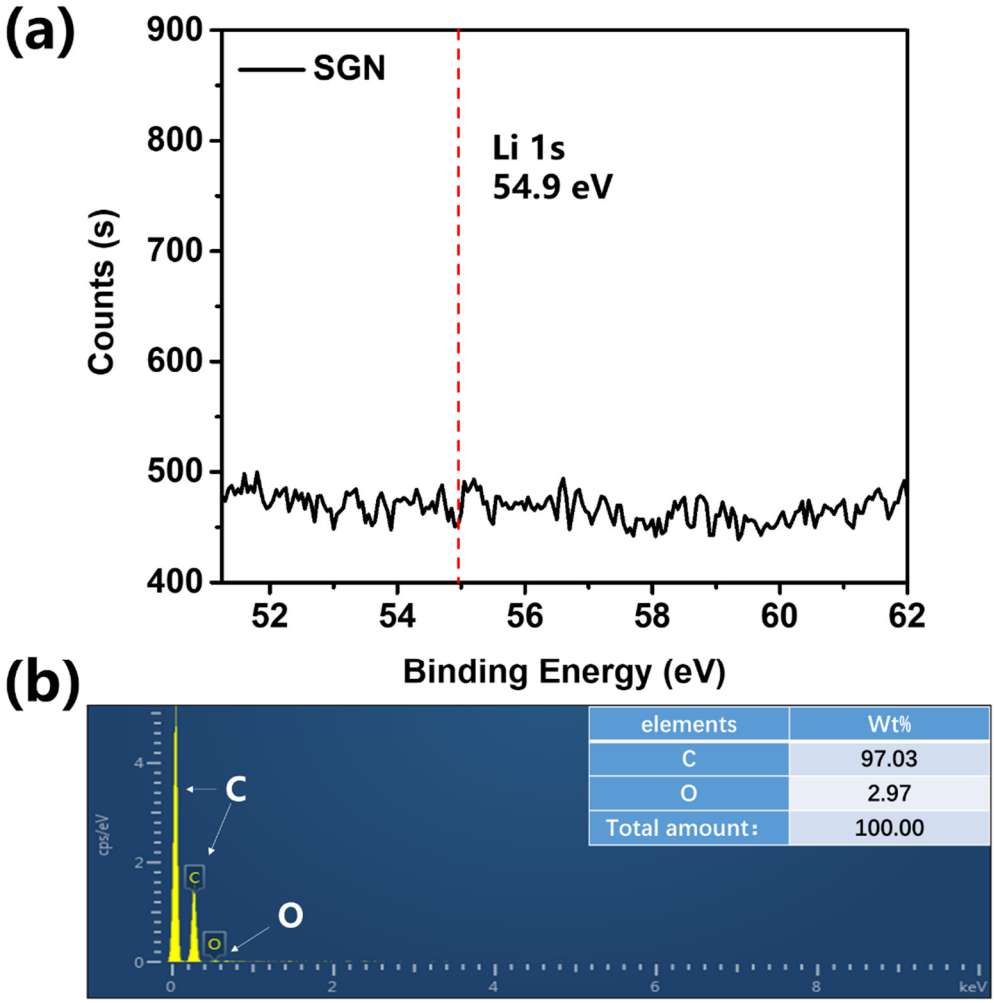

Fig. S2. (a) XPS data of the Li 1s peak for SGN. (b) The EDS spectrum of SGN.

EDS and XPS were used to analyze the elemental composition of SGN. The results show that there is no Li remaining in the SGN.

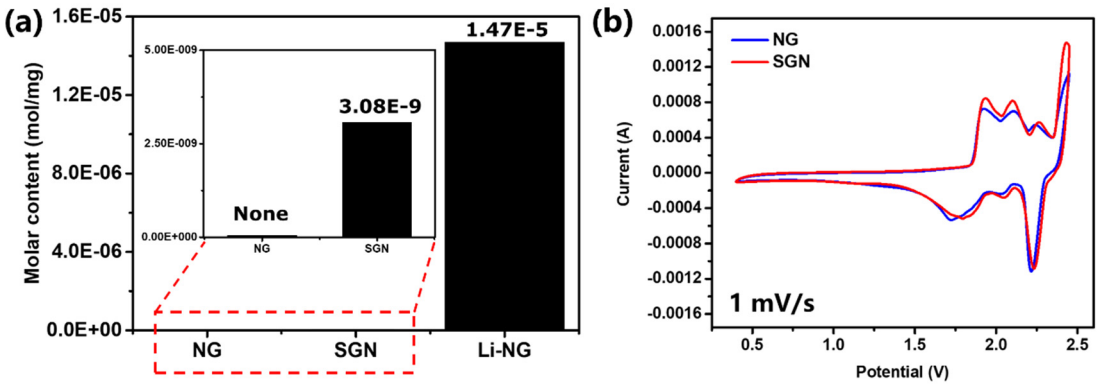

Fig. S3. (a) AAS-determined concentration of Li in NG, SGN and lithiated graphite; (b) The cyclic voltammetry curves of the NG and SGN.

To further prove no remaining lithium in the SGN sample, atomic absorption spectroscopy (AAS) was used to detect traces of lithium residues. For comparison, NG, SGN and lithiated graphite (Li-NG) samples were tested separately.

Detailed experimental process:

10 mg of material was placed in a quartz boat and heated to 900 °C for 1 h in air until the graphite was completely burned out. Afterwards, the residue in the quartz boat was completely dissolved in 5 ml of 10 % HCl solution for AAS test.

As shown in the Fig. S3a, there is only trace amount of Li in the SGN, which may be adsorbed on the surface of SGN. Theoretically, all these residue Li (3.08×10^{-9} mol/mg) on SGN can only contribute a specific capacity of 0.0825 mAh/g, if all of them could totally insert/de-insert during the charge-discharge processes. So, the effect of residue Li on the capacity of SGN can be neglected in our work.

As shown in Fig. S3b, no new redox peaks were observed in the CV curve of SGN if compared with that of the NG, which further proved that no lithium-related reactions occurred during the charge/discharge process.

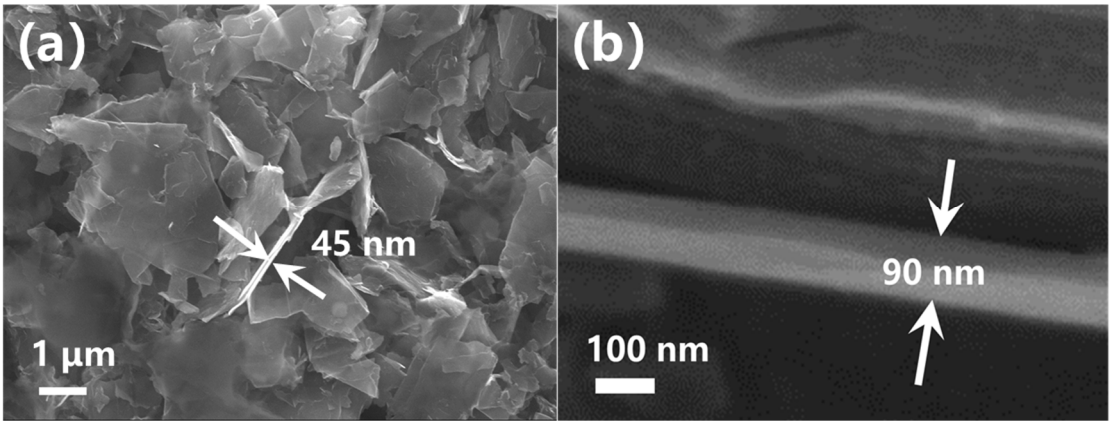

Fig. S4. SEM image of SGN (a) and NG (b).

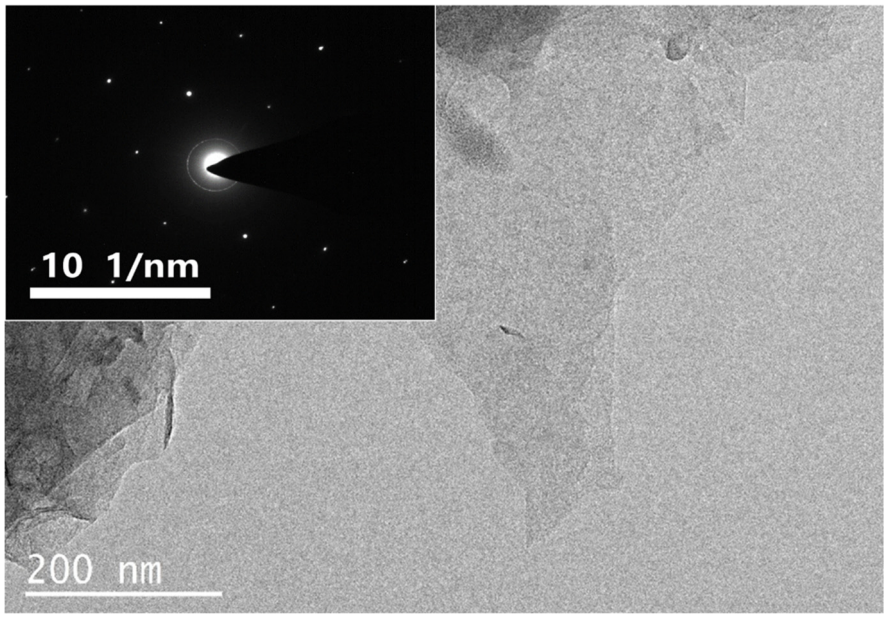

Fig. S5. TEM image of SGN (the inset is the electron diffraction pattern of SGN).

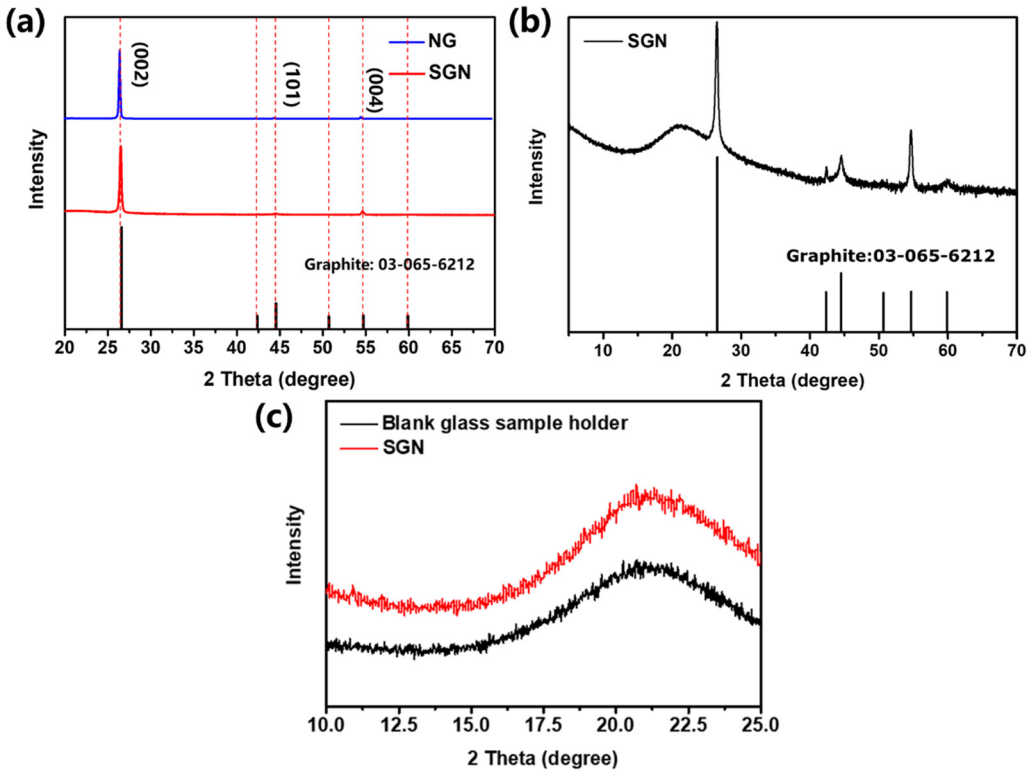

Fig. S6. (a) XRD spectra of NG and SGN (Step scan speed is 5° / min); (b) The XRD spectra of SGN in a semi-logarithmic scale; (c) The XRD spectra of SGN and blank glass sample holder from 10 ° to 25 °.

The wide peak at 20-25 degrees comes from the glass sample holder. The XRD pattern of the blank glass sample holder was also provided here (Fig. S6c).

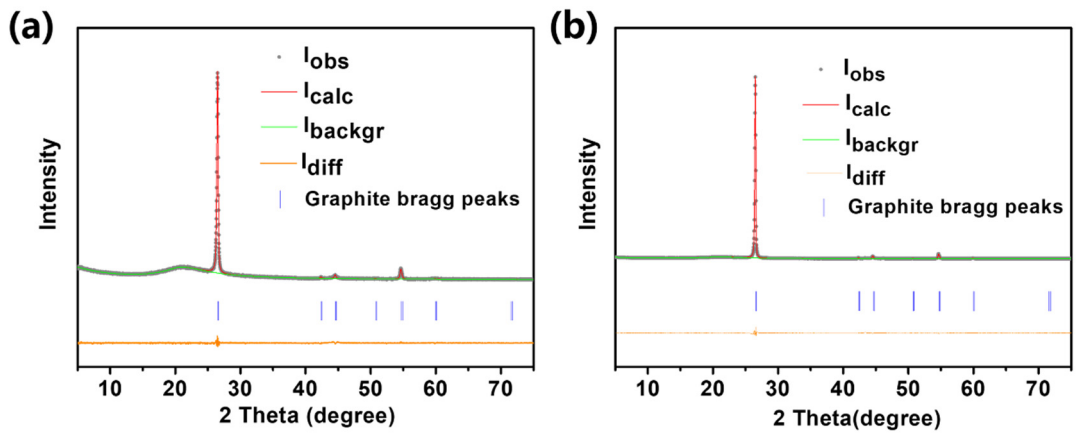

Fig. S7. Rietveld refinement of XRD spectra for SGN (a) and NG (b).

Table S1. The cell parameters and strain calculated by Rietveld refinement.

Samples	a (Å)	b (Å)	c (Å)	Strain(%)
NG	2.46109	2.46109	6.71052	0.19
SGN	2.45993	2.45993	6.70865	0.21

The very small difference in cell parameters between SGN and NG can be thought of as errors from measurement and refinement. As revealed by other works, [1] the remaining of Li into the graphite layers usually causes an obvious increase of layer spacing from 3.35 Å to 3.7 Å, and the (002) peak shifts significantly on XRD pattern. So, almost no change in cell parameters can further prove no lithium remaining in the SGN.

Besides, weak strain change can be observed in the materials. This slight microstrain may contribute to a broadening but fairly limited. Therefore, we still prefer that the decreasing number of atomic planes was the main reason for this broadening result. As revealed later in this text, a 30% leap in the FWHM for SGN was observed. Based on the Scherrer formula, such a huge change in the FWHM was primarily related to the decrease of the graphite layers.

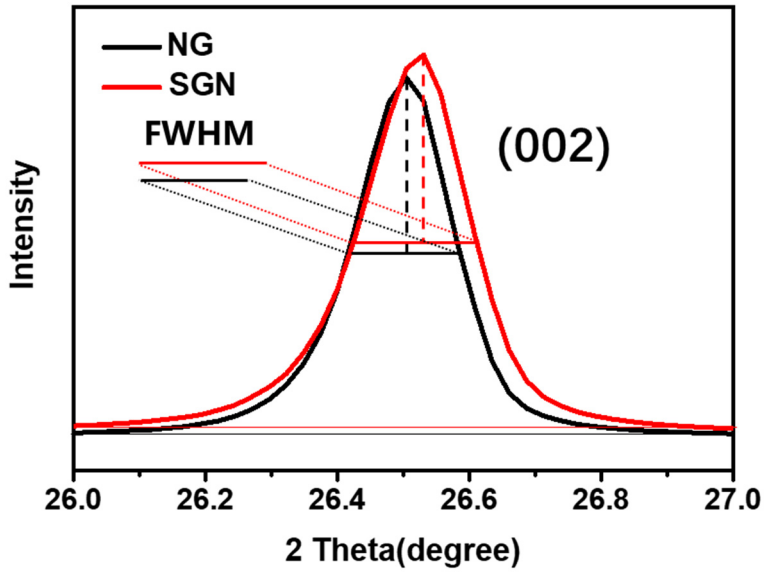

Fig. S8. (002) peaks of XRD spectra for NG and SGN.

The thickness of graphite can be estimated by the Scherrer formula, which is expressed as follows (Equation (s1)):

$$L = \frac{K\lambda}{\beta \cos\theta} \quad (s1)$$

where L is the grain size (nm), k is the Scherrer constant, λ is the X-ray wavelength (nm), θ is the half diffraction angle (degree), and β is the half height width of the diffraction peak (radian).

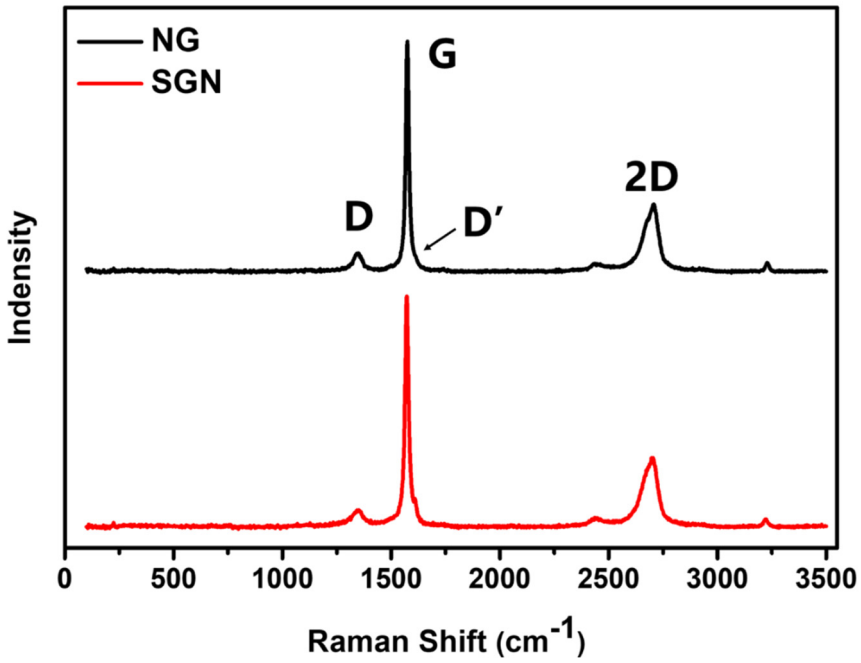

Fig. S9. Raman spectra of NG and SGN.

Raman relative peak intensity has been calculated by maximum intensity. The relative peak intensity of NG and SGN both are 0.07. If the integral intensity is used, the data for NG and SGN are 0.17 and 0.16, respectively. These two graphite samples have quite similar relative peak intensity (D/G). Besides, the small peak at 1626 cm^{-1} is the D' peak. Normally, this peak merges with the G peak as shown in the NG sample. The appearance of D' peak for the SGN is related to the break in the translational symmetry of C-C sp2 bonds, which is caused by the size reduction of graphite. [2-4]

The good performance of SGN is due not only to the more active sites brought about by its smaller size and thickness, but also to its good crystallinity maintained after the lithiation-reaction treatment in this work. Both of them are the keys to getting high capacity for graphitic carbon materials used in AIB cathode.

As is well known, structural turbulence of graphite leads to a large number of inactive defects that not only hinder the intercalation of large-size anions, but also reduce the active sites for energy storage. Furthermore, too much defect sites reduce the conductivity of the graphite. [5] Other treatments, such as ultrasonic oxidation, [6] mechanical ball milling, [7] etc., can also reduce the particle size of graphite. Unfortunately, a fatal flaw of these treatments is that such treatments are prone to producing large amounts of defects, which severely deteriorate the performance of graphite.

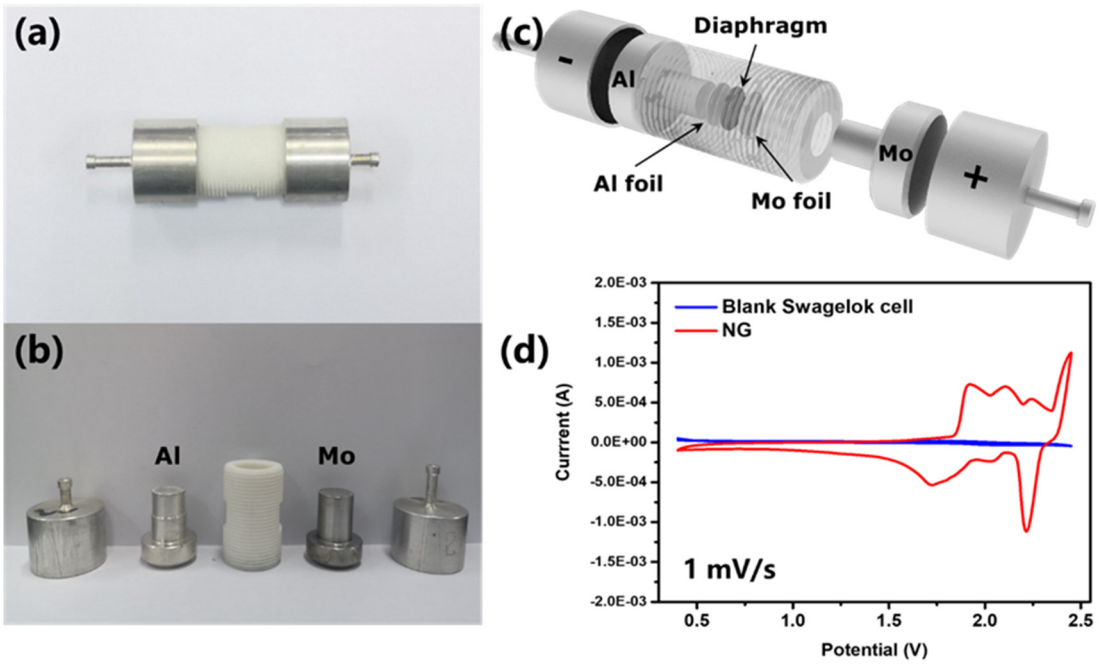

Fig. S10. Digital photo (a, b) and structure diagram (c) of the custom Swagelok cell; Cyclic voltammograms of one blank Swagelok cell without using any cathode materials and the other one assembled with a graphite cathode (d).

As shown form the Figure S10d, no redox peaks were observed in the CV curve of a blank Swagelok cell, indicating the suitability of the Swagelok cell for assembling aluminum ion battery in our work.

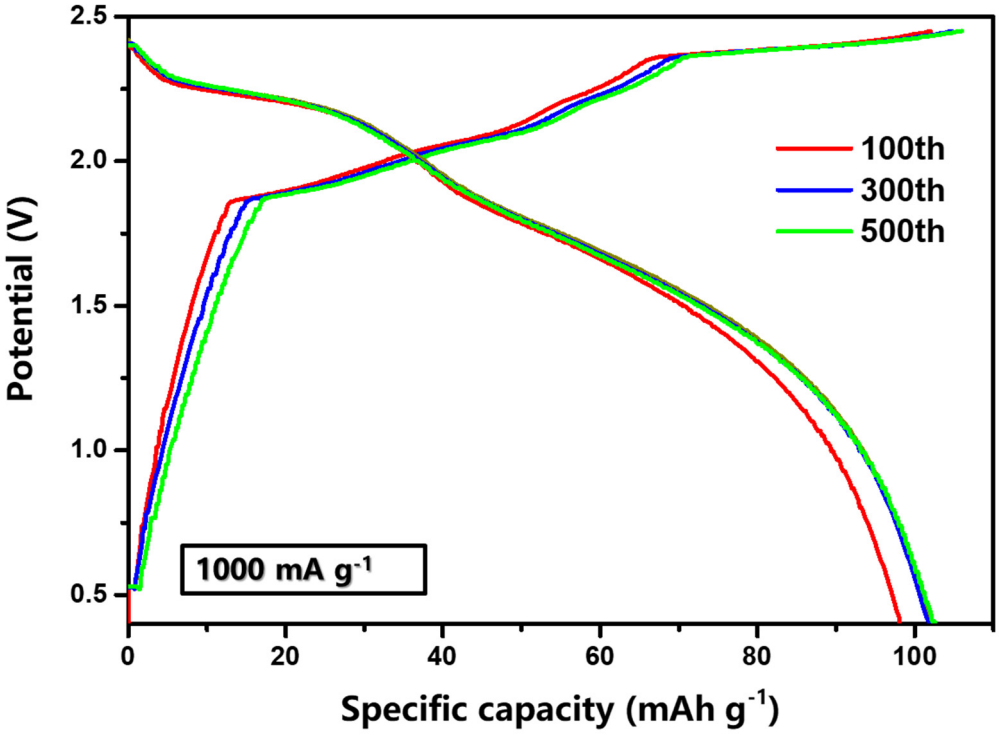

Fig. S11. Charge and discharge curves of SGN at 100th, 300th and 500th cycles.

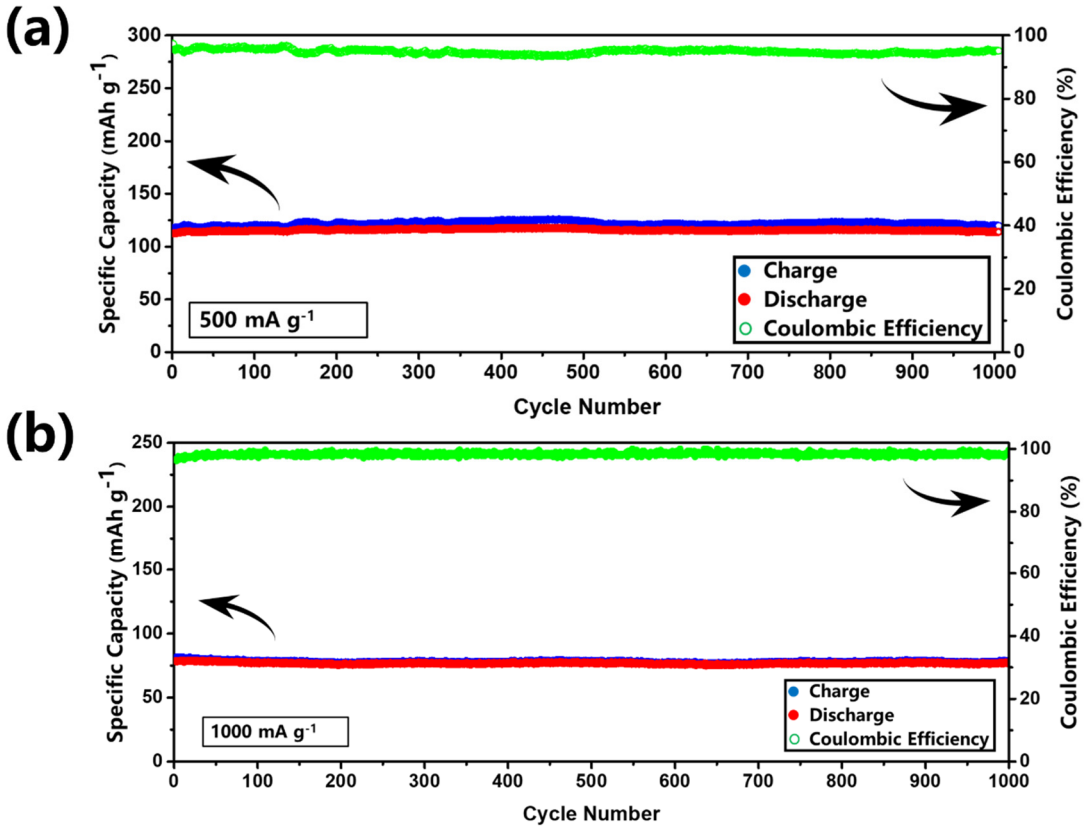

Fig. S12. (a) The cycling performance and the coulombic efficiency of SGN at a current density of 500 mA g^{-1}; (b) The cycling performance and the coulombic efficiency of NG at a current density of 1000 mA g^{-1}.

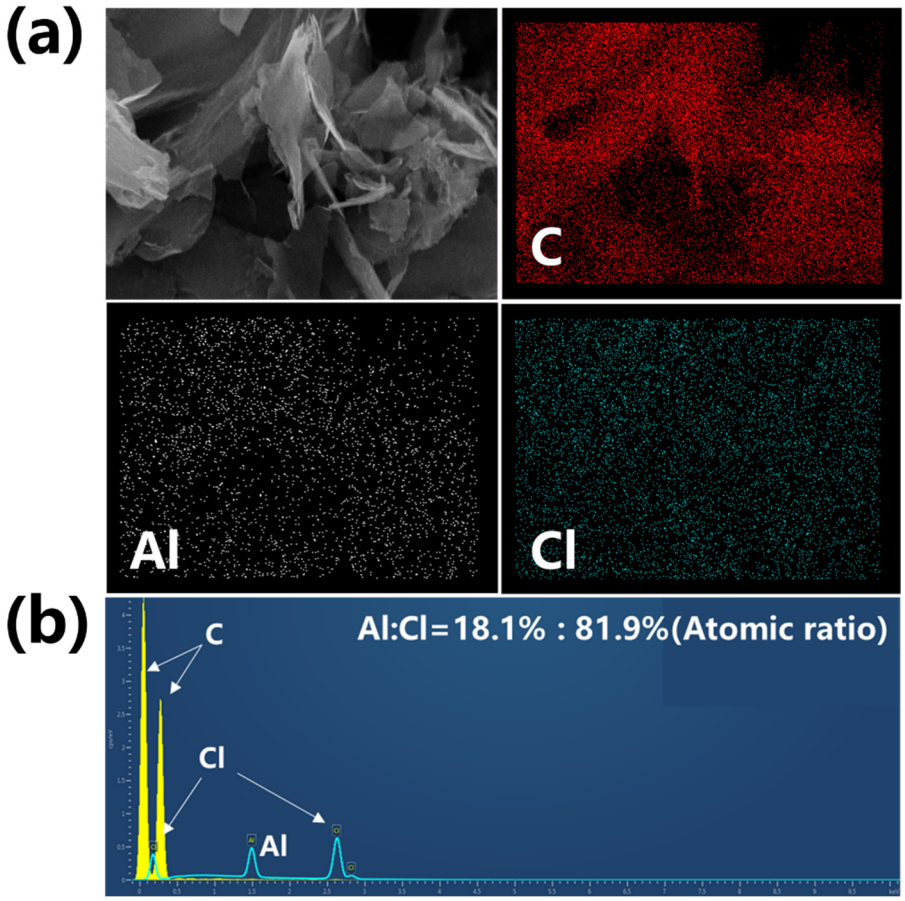

Fig. S13. (a) Elemental mapping images of C, Al and Cl for SGN sample charged to 2.45V; (b) EDS spectrum of SGN under fully charged state (2.45 V).

In order to prove that the energy storage of SGN is achieved via reversible intercalation/de-intercalation of $[AlCl_4]^-$ into/out of the graphite interlayer space, SGN is charged to 2.45V, and subjected to elemental mapping. The EDS analysis shows the Al/Cl atomic ratio of about 1/4, proving that the intercalated ion is mainly $[AlCl_4]^-$.

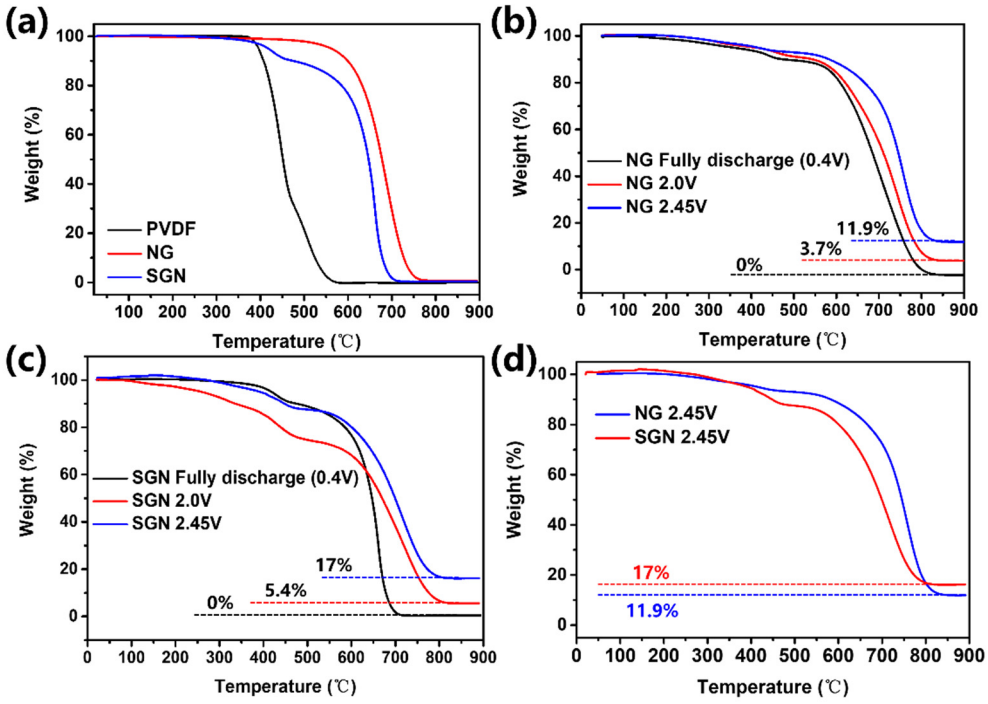

Fig. S14. TGA curves from room temperature to 890 °C at a ramping rate of 10 °C min^{-1} in air flow: (a) PVDF, SGN and NG; (b) NG at different charging states; (c) SGN at different charging states; (d) TGA curves for SGN and NG in fully charged state (2.45 V). The amount of $[AlCl_4]^-$ interposed between the graphite layers can be evaluated by the residue (Al_2O_3) of the samples at 850 ℃.

The percentages of residue mass are 0 %, 3.7 %, and 11.9 % for NG samples charged at 0.4 V, 2.0 V, and 2.45 V, respectively (Fig. S14b), and the percentages of residue mass are 0 %, 5.4 %, and 17 % for SGN samples charged at 0.4 V, 2.0 V, and 2.45 V, respectively (Fig. S14c), indicating more and more $[AlCl_4]^-$ are intercalated into graphite with the rise of charging voltage.

According to the residue mass, the value of n in $C_n[AlCl_4]$ can be calculated as follows (Equation (s2) and (s3)):

$$n_{Al} = 2i/M_{Al_2O_3} \quad \text{(s2)}$$

$$n = (100 - n_{Al}M_{AlCl_4})/M_C n_{Al} \quad \text{(s3)}$$

where i is the mass ratio of residue at 850 ºC, n_{Al} is the relative moles of Al, $M_{Al_2O_3}$, M_{AlCl_4} and M_C are the molar masses of Al_2O_3, $[AlCl_4]^-$, and C, respectively. Based on equation s2 and s3, the n values for SGN and NG at fully charged state can be estimated to be 10.9 and 22.0, respectively.

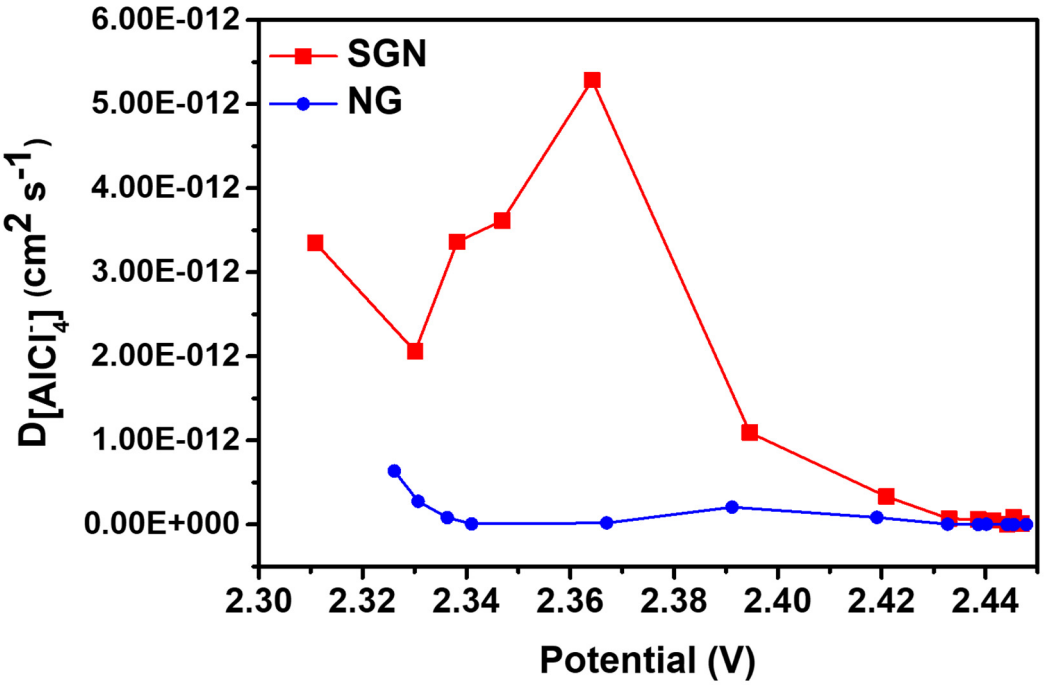

Fig. S15. The calculated $D_{[AlCl4]^-}$ from the GITT data for NG and SGN as a function of potential during the charge process (2.31-2.45V)

During the GITT test, the battery was charged with a constant current density of 100 mA g^{-1} for 5 min, then let stand in an open circuit state for 20 min to return the voltage to a steady state. During this period, the change of voltage with time is recorded. This procedure was repeated for the voltage window of 1.8-2.45V. The equation used to calculate the diffusion coefficient can be written as follows:

$$D_{AlCl_4^-} = \frac{4}{\pi}(I_0 \frac{V_m}{SFZ_i})^2 (\frac{dE/dx}{dE/d\sqrt{t}})^2 \quad \text{(s4)}$$

where V_m (cm^3 mol^{-1}) is the molar volume of the active materials, F is the Faraday constant (96485 C/mol), I_0 (A) is the applied current, S (cm^2) is the total contact area between the electrolyte and electrode, Z_i is the number of charge transferred.

In order to simplify the solution, when the applied current is very small, and the relaxation time t is very short, $dE/d\sqrt{t}$ is linear, and the above formula can be simplified as[8]:

$$D_{AlCl_4^-} = \frac{4}{\pi t}(\frac{n_m V_m}{S})^2 (\frac{\Delta E_s}{\Delta E_t})^2 \quad \text{(s5)}$$

where t is the relaxation time; n_m is the number of moles of active materials; ΔE_s is the voltage change caused by the pulse; ΔE_t is the voltage change of the constant current charge.

Table S2. Comparison of energy storage performance between small graphite nanoflakes and other AIBs graphite cathode materials.

Cathode materials	Electrolyte (molar ratio)	Discharge capacity/mAh g^{-1}		Discharge voltage plateau (V)	Ref.
		Initial discharge	last cycle (cycle number, current density)		
SGN	**1.3 : 1 $AlCl_3$: [EMIm]Cl**	**105 (1000 mA g^{-1})**	**112 (1000th, 500 mA g^{-1}) 102 (1000th, 1000 mA g^{-1})**	**2.25, 1.9**	**This work**
CF_x	0.5 : 1 $AlCl_3$: [BIm]Br	225 (60 mA g^{-1})	225 (40th, 60 mA g^{-1})	0.65	[9]
MWCNT	1.3 : 1 $AlCl_3$: [EMIm]Cl	31.3 (400 mA g^{-1})	25.8 (3500th, 400 mA g^{-1})	N/A	[10]
Pyrolytic graphite	1.3 : 1 $AlCl_3$: [EMIm]Cl	60 (66 mA g^{-1})	65 (200th, 66 mA g^{-1})	2	[11]
Carbon paper	1.3 : 1 $AlCl_3$: [EMIm]Cl	50 (150 mA g^{-1})	62.7 (50th, 150 mA g^{-1})	1.8	[12]
Graphite powder	1.3 : 1 $AlCl_3$: urea	73 (100 mA g^{-1})	73 (180th, 100 mA g^{-1})	1.9, 1.6	[13]
Nature graphite flakes	1.3 : 1 $AlCl_3$: [EMIm]Cl	60 (660 mA g^{-1})	60 (200th, 660 mA g^{-1})	2.25-2.0, 1.9-1.5	[14]
Graphitic carbon paper	1.63 : 1 $AlCl_3$: NaCl (120℃)	64.9 (4000 mA g^{-1})	43 (9000th, 4000 mA g^{-1})	1.9, 1.25	[15]
3D graphene mesh network	1.3 : 1 $AlCl_3$: [EMIm]Cl	57 (2400 mA g^{-1})	55.5 (200th, 2400 mA g^{-1})	2.0	[16]
3D graphitic foams	1.3 : 1 $AlCl_3$: [EMIm]Cl	60 (12000 mA g^{-1})	60 (4000th, 12000 mA g^{-1})	1.8	[17]
Graphitic-foam	1.3 : 1 $AlCl_3$: [EMIm]Cl	60 (5000 mA g^{-1})	60 (7500th, 5000 mA g^{-1})	2	[11]
Commercial expanded graphite	1.3 : 1 $AlCl_3$: EMI	85 (1000 mA g^{-1})	60 (3000th, 1000 mA g^{-1})	2.25, 1.9	[18]
Commercial expanded graphite	1.3 : 1 $AlCl_3$: ET	78.3 (5000 mA g^{-1})	60 (30000th, 5000 mA g^{-1})	2.1, 1.8	[18]

References

1. T. Nonaka, H. Kawaura, Y. Makimura, Y. F. Nishimura and K. Dohmae, *Journal of Power Sources*, 2019, **419**, 203-207.
2. I. Clemente, A. Miakonkikh, O. Kononenko, V. Matveev and K. Rudenko, *Journal of Physics Conference Series*, 2017, **917,** 032039.
3. A. Eckmann, A. Felten, A. Mishchenko, L. Britnell, R. Krupke, K. S. Novoselov and C. Casiraghi, *Nano letters*, 2012, **12**, 3925-3930.
4. S. C. Ray, *Frontier Research Today*, 2018, **1**, 1002.
5. H. Chen, F. Guo, Y. Liu, T. Huang, B. Zheng, N. Ananth, Z. Xu, W. Gao and C. Gao, *Advanced materials*, 2017, **29**, 1605958.
6. T. Soltani and B. Kyu Lee, *Journal of Colloid and Interface Science*, 2017, **486**, 337-343.
7. A. Pragatheeswaran, R. Ravi and S. R. Bakshi, *Advanced Powder Technology*, 2019, **30**, 2759-2767.
8. Z. Shen, L. Cao, C. D. Rahn and C.-Y. Wang, *Journal of The Electrochemical Society*, 2013, **160**, A1842-A1846.
9. J. V. Rani, V. Kanakaiah, T. Dadmal, M. S. Rao and S. Bhavanarushi, *Journal of The Electrochemical Society*, 2013, **160**, A1781-A1784.
10. H. Jiao, J. Wang, J. Tu, H. Lei and S. Jiao, *Energy Technology*, 2016, **4**, 1112-1118.
11. M.-C. Lin, M. Gong, B. Lu, Y. Wu, D.-Y. Wang, M. Guan, M. Angell, C. Chen, J. Yang, B.-J. Hwang and H. Dai, *Nature*, 2015, **520**, 324.
12. H. Sun, W. Wang, Z. Yu, Y. Yuan, S. Wang and S. Jiao, *Chemical Communications*, 2015, **51**, 11892-11895.
13. M. Angell, C.-J. Pan, Y. Rong, C. Yuan, M.-C. Lin, B.-J. Hwang and H. Dai, *Proceedings of the National Academy of Sciences*, 2017, **114**, 834-839.
14. D. Y. Wang, C. Y. Wei, M. C. Lin, C. J. Pan, H. L. Chou, H. A. Chen, M. Gong, Y. Wu, C. Yuan and M. Angell, *Nature Communications*, 2017, **8**, 14283.
15. Y. Song, S. Jiao, J. Tu, J. Wang, Y. Liu, H. Jiao, X. Mao, Z. Guo and D. J. Fray, *Journal of Materials Chemistry A*, 2017, **5**, 1282-1291.
16. G. Yang, L. Chen, P. Jiang, Z. Guo, W. Wang and Z. Liu, *RSC Advances*, 2016, **6**, 47655-47660.
17. Y. Wu, M. Gong, M. C. Lin, C. Yuan, M. Angell, L. Huang, D. Y. Wang, X. Zhang, J. Yang, B. J. Hwang and H. Dai, *Advanced Materials*, 2016, **28**, 9218-9222.
18. X. Dong, H. Xu, H. Chen, L. Wang, J. Wang, W. Fang, C. Chen, M. Salman, Z. Xu and C. Gao, *Carbon*, 2019, **148**, 134-140.